



HAL
open science

Effect of the Thermal History on Macrostructure and Microstructure Development in High-Strength Steel Welds

Nicolas Jousset, Marine Gaumé, Florent Bridier, Julien Beaudet, Jean-Loup Heuzé, Anne-Françoise Gourgues-Lorenzon

► **To cite this version:**

Nicolas Jousset, Marine Gaumé, Florent Bridier, Julien Beaudet, Jean-Loup Heuzé, et al.. Effect of the Thermal History on Macrostructure and Microstructure Development in High-Strength Steel Welds. Metallurgical and Materials Transactions A, 2022, 53, pp.2561-2576. 10.1007/s11661-022-06686-2 . hal-03649371

HAL Id: hal-03649371

<https://minesparis-psl.hal.science/hal-03649371>

Submitted on 22 Apr 2022

HAL is a multi-disciplinary open access archive for the deposit and dissemination of scientific research documents, whether they are published or not. The documents may come from teaching and research institutions in France or abroad, or from public or private research centers.

L'archive ouverte pluridisciplinaire **HAL**, est destinée au dépôt et à la diffusion de documents scientifiques de niveau recherche, publiés ou non, émanant des établissements d'enseignement et de recherche français ou étrangers, des laboratoires publics ou privés.



Distributed under a Creative Commons Attribution - NonCommercial - NoDerivatives 4.0 International License

EFFECT OF THE THERMAL HISTORY ON MACROSTRUCTURE AND MICROSTRUCTURE DEVELOPMENT IN HIGH STRENGTH STEEL WELDS¹

Nicolas JOUSSET^{1,2*}, Marine GAUME², Florent BRIDIER², Julien BEAUDET², Jean-Loup HEUZE³, Anne-Françoise GOURGUES-LORENZON¹

¹ MINES ParisTech, PSL University, MAT – Centre des Matériaux, CNRS UMR 7633, BP87 91003 Evry Cedex, France

² Naval Group RESEARCH – CESMAN TechnoCampus Océan, 44340 Bouguenais, France

³ Ministère des Armées / DGA – BALARD, 75509 Paris Cedex 15, France

*Corresponding author: nicolas.jousset@mines-paristech.fr

Abstract

The present work addresses the microstructural and macrostructural development in multipass welded joints. It focuses on multiple thermal cycles induced by successive deposition of welding passes. The local welding-related thermal history was related in detail to the evolution of austenite grains during manufacturing of two high-strength low-alloy steel welds. The analytical Rosenthal thermal model was used to identify the thermal cycles experienced within typical weld metal regions. Selected heat cycles were applied to laboratory specimens, taken from the same weld metal, to investigate microstructural evolution during the welding process. Heat cycle experiments, involving full austenitization, showed the persistence of columnar zones resulting from a memory effect of the prior austenite grains during the reverse transformation. Intercritical heat cycles led to white-etching, softer regions with high fractions of retained austenite. They also showed that the memory of austenite grains was actually stored in elongated retained austenite particles that remained after complete welding. This memory effect vanished under high peak temperatures (typically, 130°C higher than A_{c3}); this was linked to a competition between growth and merging of elongated, intragranular retained austenite particles, and growth of equiaxed, intergranular austenite particles. Finally, a low peak temperature promoted refined, harder final microstructures.

Keywords: high-strength steel, multipass weld, bainite, martensite, austenite memory, thermal history

¹ This is the accepted version of the paper published in Metall. Mater. Trans. (2022), with the following doi identifier: <https://doi.org/10.1007/s11661-022-06686-2>; Copyright for the publisher's version: The Minerals, Metals & Materials Society and ASM International 2022

1 Introduction

High strength steels are widely used in structural parts and an optimization of their microstructures allows a good combination of mechanical strength and toughness [1-4]. To assemble these structural parts, manual arc welding offers great flexibility and can be used in all welding positions. It is often used to produce multipass welds joining thick-walled components, i.e., with a large number of weld beads.

The microstructural design of multipass weldments mainly focused on the heat affected zone (HAZ), which in many cases is the most brittle region of the weld due to the formation of local brittle zones [5-7]. Fewer studies addressed the weld metal itself in high strength multipass welds. It contains regions that are reheated and thus austenitized several times by the passes deposited either above or next to them. The determination of the thermal history experienced by the material in different regions of multipass welded joints is therefore challenging. To this aim, numerous analytical and numerical models have emerged, ranging from single point heat sources [8-9] to complex heat sources with models incorporating thermal-mechanical-microstructural predictions [10]. These models have mostly been used to estimate residual stresses and distortions that develop during welding and to estimate the morphology of welding passes. They have been as well used to estimate local thermal cycles in the weld metal or HAZ [11]. On the other hand, macrographs of real welds are mainly used to validate the morphology of passes predicted by numerical models, but they are rarely used to extract information about the local thermal history.

Up to now, the influence of thermal history has mainly been addressed through the effect of the cooling rate [12-14] or the welding parameters on the microstructural evolution of the weld metal [15-17]. However, the influence of peak temperature variations has rarely been reported in weld metal [18-20]. The effect of the peak temperature on the prior austenite γ grain size (PAGS) and then on the final microstructure can be of primary importance as shown by many studies on the HAZ, which investigated the differences between coarse-grained, fine-grained and inter-critically reheated regions through simulated heat cycles [5-7,21-22].

In a multipass weld metal, several regions can be outlined in macrographs by their different prior austenite grain morphology. These regions are commonly classified as columnar vs. equiaxed (with fine-grained and coarse-grained zones) [19,20,23-25]. It is also common to differentiate reheated regions, which are thermally affected by further metal deposition, from as-deposited regions. However, this terminology may be confusing because as-deposited regions are sometimes referred to as top bead/unaffected microstructures [12], and sometimes as the columnar regions [19,25-28]. More precisely, columnar regions are often considered to never experience temperatures higher than Ac_3 (end temperature of the austenite transformation on heating) after deposition, whereas equiaxed regions are considered as fully austenitized at least once during reheating. However, very little work has been reported to support this theoretical knowledge of the local thermal history in a multipass weld. In fact, columnar zones may be significantly reheated without losing their columnar morphology [24,29]. The evolution and inheritance of austenite morphology through a reverse transformation have been the subject of many studies in Fe-Ni alloys [30,31], Fe-Cr-Ni alloys [32-34], and martensitic/bainitic low alloy steels [35-38]. To the authors' knowledge, the link between morphological evolution of austenite grains and the heat cycle conditions involved by reheating has not yet been reported in the literature regarding multipass welds.

The studies on base metals revealed a heredity of the morphology of prior austenite grains during the reverse α' (martensite/bainite) $\rightarrow \gamma$ (austenite) phase transformation. In the literature, this phenomenon has been referred to as “austenite memory”: under certain conditions, reverted austenite keeps identical grain shape, size and crystal orientation as those of the parent austenite that decomposed into the starting microstructure (referred to as the “initial austenite” in the following). Several possible mechanisms have been proposed in literature to explain the austenite memory during the reverse phase transformation:

- 1) Martensitic-like reverse transformation with a diffusionless shear mechanism [30,31,37-39];
- 2) Variant selection of reverted austenite, with respect to crystal orientation of neighboring cementite and martensitic laths [40,41];
- 3) Diffusional growth of retained austenite that kept the orientation of initial austenite grains [32,42];
- 4) Variant selection from orientation relationships between martensitic laths and reversed austenite, influenced by an internal stress field [32,34,39].

The present work aims at improving current understanding of the influence of local thermal history (in particular of peak temperature) on the macrostructure and final microstructure of multipass welds. The thermal history was estimated using numerical and analytical tools. Macrographs from actual welded joints were then used to determine thermal histories in selected regions. The link between heat cycle and final microstructure was then confirmed using selected laboratory heat cycles with different peak temperatures. The methodology addressed alternating columnar and equiaxed austenite grain morphology (so, the presence of austenite memory) as well as white etching bands. The effect of the peak temperature on the microstructure after the final decomposition of austenite was also investigated.

2 Experimental procedure

2.1 Experimental welds

Two high-strength steel welds were fabricated by multipass shielded metal arc welding using the same low carbon, low alloy filler material. The same preheat/interpass temperature was used for the two welds together with different welding heat input (HI) energy levels, respectively, a lower value (LowHI) and a higher value (HighHI). The chemical composition of the weld metal is shown in Table I.

Table I - Chemical composition of the weld metal.

	C	Si	Cr	Mn	Ni	Mo	Fe
Weld metal (wt.%)	<0.1	<0.60	<0.70	<1.85	<2.00	<0.95	Bal.

The macrographs of the two welded joints are presented in Figure 1 and Figure 2, respectively, after a 2% nital etching and after a Béchét-Beaujard etching. In order to minimize dilution-induced artifacts, only regions of the welds located far from the base metal were considered. For the same reason, the last pass was deposited at mid-width of the weld, as shown in Figure 1 and Figure 2.

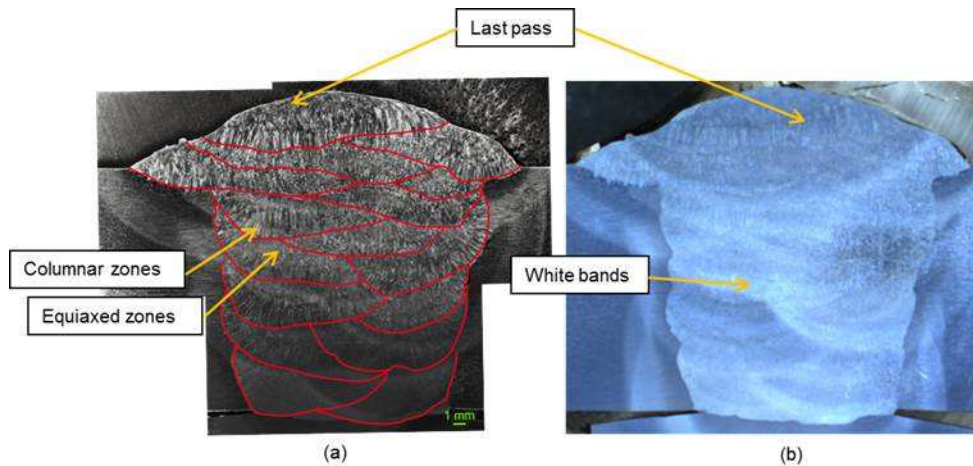


Fig. 1 - Macrographs of the HighHI weld (a) after a 2% nital etching with fusion lines outlined in red continuous lines, (b) after a Béchet-Beaujard etching.

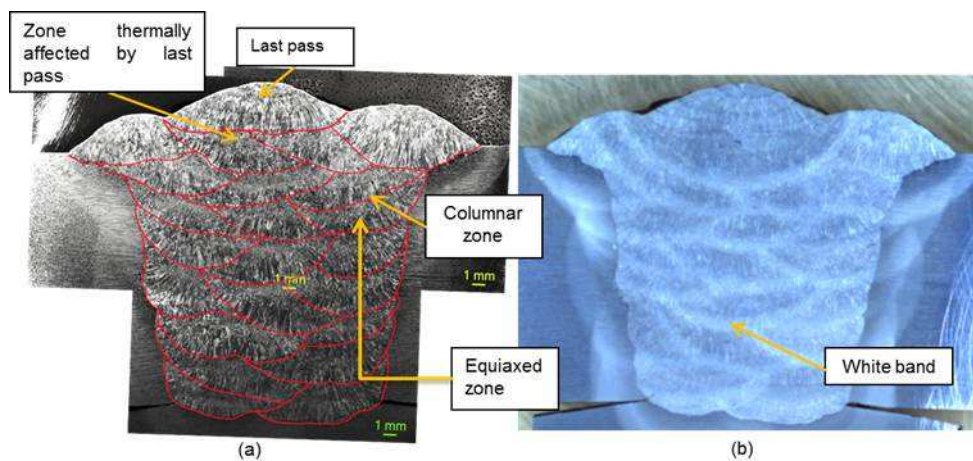


Fig. 2 - Macrographs of the LowHI weld (a) after a 2% nital etching with fusion lines outlined in red continuous lines, (b) after a Béchet-Beaujard etching.

2.2 Laboratory heat cycles

The Rosenthal analytical model was used to estimate the thermal history of the considered multipass welds and to extract information to design the experimental campaign. This simplified model readily gives results consistent with experimental data in many cases [43,44]. It involves strong assumptions: the heat source is assimilated to a moving single point source, thermal-physical material properties do not depend on temperature, and there is no heat loss from the surface of the work piece (either by convection or by radiation). This approach is mostly used to estimate temperature evolutions in reheated zones (either HAZ or affected passes in the weld metal) [19]. It allows the temperature to be immediately obtained as a function of time, at a given distance from the heat source, only taking thermal conduction within the welded part into account.

Thanks to the use of the Rosenthal model, hypotheses were made about the origin of the different zones observed in macrographs (i.e., columnar zones, equiaxed zones, white bands). To test these hypotheses, several typical heat cycles were applied to samples extracted from these welds.

The experimental heat cycles were applied using a quenching dilatometer. Two types of specimens (3 mm and 5 mm in diameter) were machined entirely in the weld metal of the HighHI weld, out of the dilution, parallel to the welding direction. A preliminary study revealed no discrepancy between

microstructures obtained using either the 3-mm or the 5-mm-diameter specimen geometry. Heat cycles were applied using a radiation furnace under air vacuum, and helium was used for cooling, the specimen temperature being monitored using a K-type thermocouple spot-welded onto the specimen surface.

The heat cycles were selected to approximate real welding conditions thanks to the thermal analysis under the actual welding conditions. The values of A_{c1} and A_{c3} , respectively start and end temperature of the austenite transformation on heating, were first determined to 690°C and 840°C, respectively, for the considered heating conditions. Four tests were then performed for a better understanding of the microstructural development: two cycles with a peak temperature, T_{peak} , higher than A_{c3} , and two cycles with a peak temperature lower than A_{c3} (intercritical (IC) reheating) (Figure 3).

The same cooling scheme was prescribed for all tests: 12 °C/s down to 500 °C and then 5 °C/s down to room temperature. These simplified conditions were representative of cooling paths predicted by thermal modeling, especially, close to the temperature range corresponding to decomposition of austenite (between 480°C and 380°C). Table II and Figure 3 show the testing conditions for each cycle. The fractions of martensite and bainite were calculated by applying the lever rule method to dilatometric curves.

Table II - Testing conditions for each laboratory heat cycle.

T_{peak} (°C)	Heating rate (°C/s)	Cooling rates	Objective
1050	80	12 °C/s ($T > 500$ °C) 5 °C/s ($T < 500$ °C)	Influence of the peak temperature on the final microstructure and austenite memory
870	60		
805	50		Austenite memory mechanism
720	50		

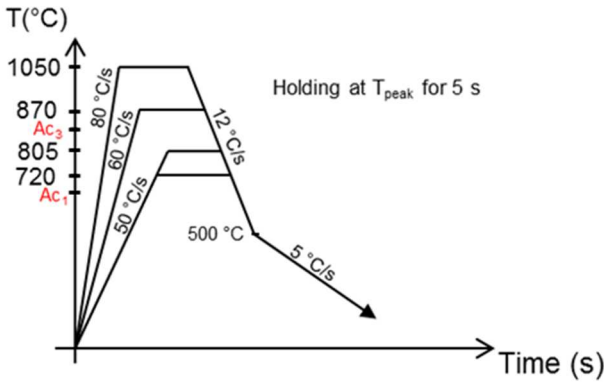


Fig. 3 – Schematic diagram presenting laboratory heat cycles.

2.3 Microstructural investigations

The microstructures were observed using a binocular magnifier, an optical microscope and a Zeiss Sigma 300 field emission gun Scanning Electron Microscope (SEM) operated in secondary electron imaging mode. The specimens were cut perpendicular to the welding direction, and close to the welded thermocouple in the case of laboratory heat-treated specimens. They were ground with fine

grit silicon carbide papers and polished with diamond pastes. Two chemical etchants were used to reveal the macrostructure and the microstructure, namely, 2% nital and Béchét-Beaujard reagents. EBSD (Electron Back-Scattered Diffraction) was performed on a HighHI sample after 0.05 μm silica suspension polishing under the following conditions: acceleration voltage, 20 kV; tilt angle, 70°; step size, 0.4 μm ; magnification, 250X; size, 340x340 μm . The crystallographic orientation information data were then analyzed with TSL OIM software. EBSD maps were used to identify parent austenitic grains using {001} pole figures by considering the characteristic features of Bain zones that result from the decomposition of austenite into bainite or martensite. The correlation between austenitic grain identification from EBSD maps and optical micrographs after a Béchét-Beaujard etching was very good.

The microstructures presented in this work were complex and composed of different micro-constituents. The presence of retained austenite is common in high-strength steel welds [15, 45], well identified with its elongated morphology, its relief after chemical etching and its localization mostly along lath boundaries. Some particles from a weld metal, having the same chemistry and fabricated under similar welding conditions as in the present work, were analyzed by Transmission Electron Microscopy in another part of the research project not detailed here [46]). They were unambiguously identified as retained austenite using selected area electron diffraction.

To classify the other microstructural constituents in the SEM micrographs (bainite, martensite), the transformation temperatures during cooling as well as local hardness values gave clear evidence to differentiate bainite (<380 HV) from martensite (>400 HV). The morphology of laths and of secondary phases was also used to differentiate the microstructural constituents (e.g., granular bainite from upper bainite) according to the classification scheme for microstructural constituents proposed by Zajac et al. in [47].

Electron probe microanalysis (EPMA) elemental mapping analysis were performed using a Cameca SX100 device on a HighHI sample after 1 μm diamond polishing. The local chemical composition was analyzed over a 300x300 μm^2 map with the following operating conditions: 15 kV accelerating voltage, 80 nA current, 1 μm step size and 20 s time analysis on each measured point.

The final microstructures were also characterized using Vickers microhardness profiles with a 0.3 kg weight and a dwell time of 10 s.

3 Results

3.1 Interpretation of macrographs

Several typical zones were identifiable in macrographs, namely: the last pass and its affected zone (Figure 4), columnar and equiaxed regions (Figure 1(a) and Figure 2(a)), and white etching bands (“white bands” hereafter) (Figure 1(b) and Figure 2(b)).

To investigate the origin of these regions, the Rosenthal model was used to estimate iso- T_{peak} lines from distance measurements in macrographs. To do so, the evolution of T_{peak} with the distance from the heat source was calculated for both welding conditions. The method is illustrated for the LowHI condition in Figure 4(b). It was based on distances to a reference iso- T_{peak} line, for which T_{peak} could be unambiguously determined. This reference was the liquidus temperature, corresponding to the fusion line, i.e., to the lower boundary of columnar regions in macrographs.

Similar results were obtained for the two welded joints; they are mostly discussed in detail for the LowHI conditions in the following.

3.1.1 Last pass: as-deposited material

As-deposited microstructures were investigated using the last pass. From its chemical composition, the studied low carbon, low alloy steel solidified into δ ferrite. From the macrograph, it solidified into columnar grains and then into equiaxed grains on the upper part of the last pass. The transition between columnar-etching and equiaxed-etching grains is visible in Figure 4. Here, we focus on the top regions of Figure 4(a). EBSD analysis of an as-deposited columnar-etching zone (Figure 5) showed the presence of columnar austenite grains. The size of the columnar austenite grains was similar to that of columnar grains in macrographs after nital etching (Figure 4). Figure 6 displays several columnar austenitic grains (delineated by thin dark lines) together with the location of interdendritic segregations in an optical micrograph.

The local chemical composition was studied between interdendritic regions and dendritic core regions with EPMA analysis. Figure 7(a) shows the investigated zone with the presence of interdendritic regions in dark-etching lines (after Béchet-Beaujard etching). EPMA elemental maps (Figure 7(b)) shows clear evidence of local chemical segregation. Austenite forming elements such as Ni and Mn as well as other alloying elements (Mo, Si, and Cr) were present in larger amounts in brighter regions which are, by comparison with the micrograph in Figure 7(a), the interdendritic regions. Thus, the solidification sub-structure spatially coincided with the local chemical segregation.

From larger-scale observations, the orientation of interdendritic segregation in this region suggests the presence of only one δ ferrite solidification grain. As illustrated in Figure 6, the δ ferrite solidification grains obviously contained several austenite grains. Consequently, columnar-etching grains in macrographs were assimilated to austenite grains, inherited from δ ferrite columnar grains. Similar observations (not illustrated here) showed equiaxed austenite grains in the equiaxed-etching regions. These results revealed that upon solidification, the morphology of δ ferrite grains was somehow transmitted to austenitic grains during the $\delta \rightarrow \gamma$ phase transformation. Moreover, the size of columnar-etching austenite grains was rather uniform all over the welds, whatever the thermal affectation by successive passes. This suggests some persistent memory effect of the austenite grains of the *as-deposited* microstructure.

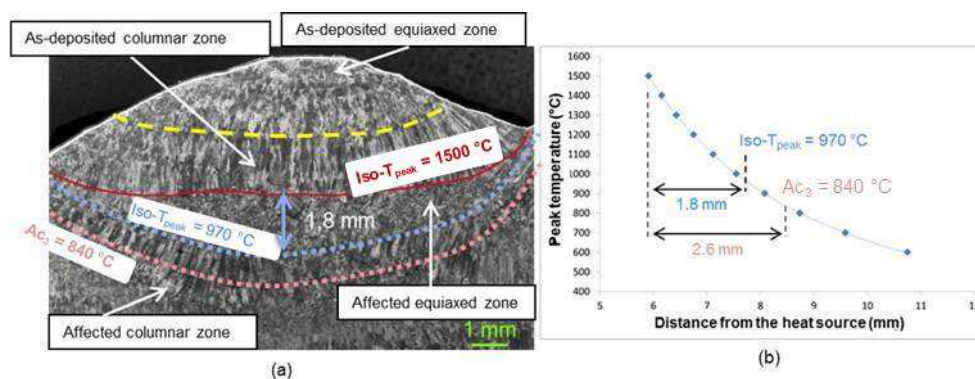


Fig. 4 – (a) Macrograph of top part of the LowHI weld with iso-T_{peak} lines of interest, including the columnar/equiaxed transition of austenitic grains in the region affected by the last pass. The values of T_{peak} are indicated close to the corresponding lines. (b) Estimation of the value of T_{peak} corresponding to that transition, using the Rosenthal model.

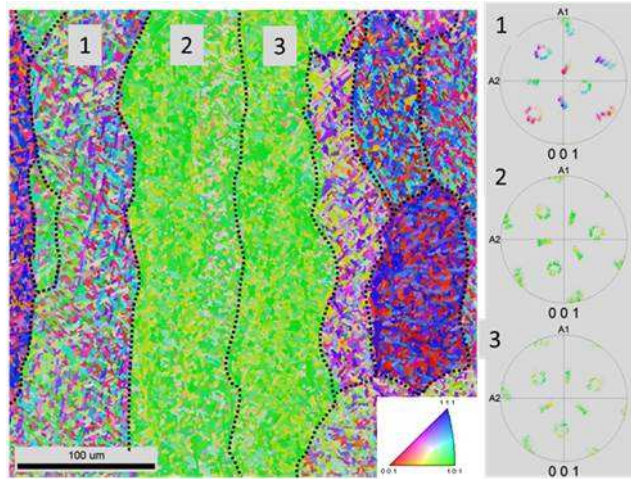


Fig. 5 – EBSD maps of a region in the as-deposited columnar zone of the last pass of the HighHI weld. Inverse pole figure map along the welding direction and illustration of the {001} pole figures of several as-deposited austenite grains with the three Bain zones of the austenite decomposition products; austenite grains are delimited by dotted lines for better readability.

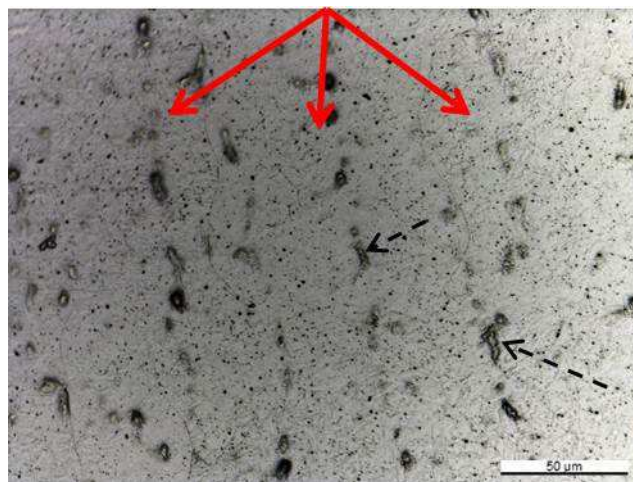


Fig. 6 – Optical micrograph showing darker interdendritic regions (dotted black arrows). Continuous red arrows show columnar austenitic grain boundaries within a single solidification grain.

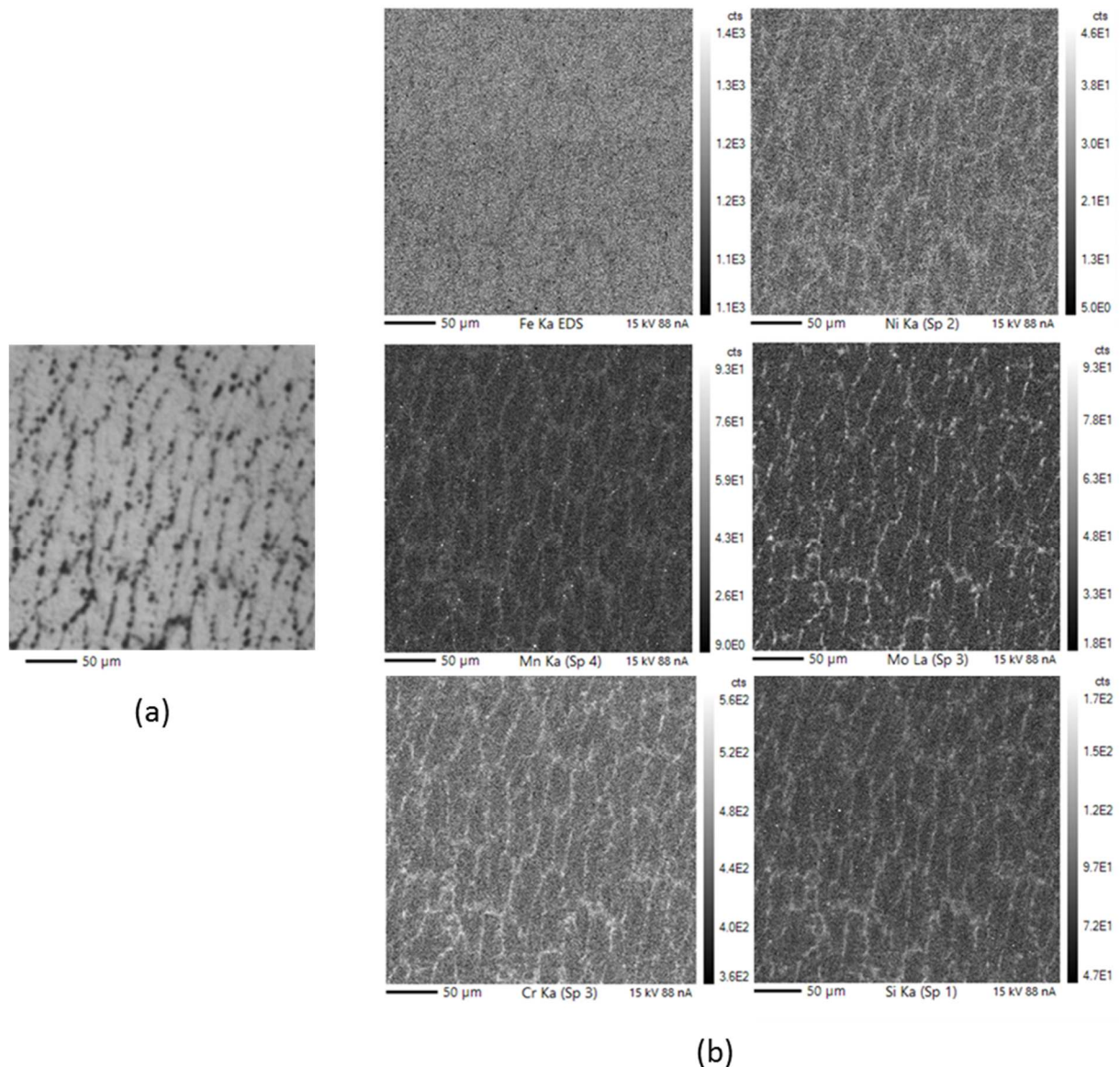


Fig. 7 – (a) Optical micrograph of EPMA investigated zone (HighHI weld), after Béchet-Beaujard etching revealing interdendritic regions, (b) EPMA elemental maps of alloying elements in the same region (step size: 1 μm).

3.1.2 Region affected by the last welding pass

In the macrograph of the region affected by the last welding pass (bottom two regions in Figure 4(a)), equiaxed-etching grains and columnar-etching grains were respectively observed close to, and far from the last pass. The Rosenthal model was used to interpret this alternation. The fusion line ($T_{\text{peak}} = 1500 \text{ }^\circ\text{C}$) was located in the macrograph; then, the $\text{iso-}T_{\text{peak}}$ line corresponding to A_{c3} ($840 \text{ }^\circ\text{C}$) (“austenitization boundary” hereafter) was located by using the Rosenthal model (Figure 4(b)). In the macrograph of Figure 4(a), the austenitization boundary was located right in the middle of the columnar region. This means that the transition between columnar and equiaxed austenite grains did *not* correspond to the transition between partial and full austenitization of the affected region. To better understand that transition in austenite grain morphology, the value of T_{peak} line corresponding to the transition was also identified in the macrograph (dashed blue line in Figure 4) and the distance to the liquidus line was reported in the curve issued from the Rosenthal model (Figure 4(b)). The corresponding value of T_{peak} was estimated to 970°C . It reveals a change in the

morphology of the parent grains for a peak temperature significantly higher (+130°C) than A_{c3} . These findings strongly support the hypothesis of austenite memory well after reaching full austenitization by affecting passes.

3.1.3 White bands

White bands appeared after chemical etching. Their upper boundary was readily determined (Figure 8). These bands followed thermal affectation by each welding pass, as shown by the correlation between the white bands and fusion lines of each affecting pass in Figure 8. This is particularly obvious for the white band created by the last pass.

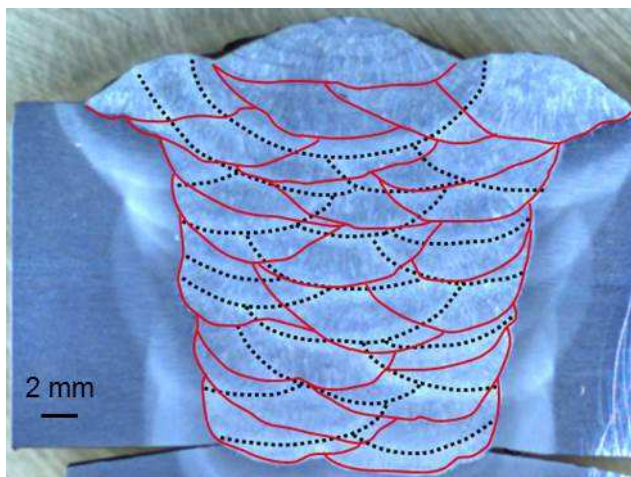


Fig. 8 – LowHI weld macrograph with the fusion lines (continuous lines) and the top boundary of white bands (dotted lines). Béchét-Beaujard etching.

The value of T_{peak} corresponding to the top boundary of white bands was estimated from iso- T_{peak} lines (dotted lines in Figure 8) with the Rosenthal model, for all white bands of the two welds. The resulting average value of T_{peak} was 750 °C. This value is well within the intercritical range, i.e., between A_{c1} (690 °C) and A_{c3} (840 °C). Similar values were found for any white bands of the HighHI weld (Table III). They indicate a similar heat cycle for all white bands: the last austenitization experienced from affectation by the next passes was partial. The lower limit of white bands was more blurry in the macrographs (Figure 8), so that it was not studied using this method.

Table III - White bands temperature estimation for LowHI and HighHI weld. Intervals reflect the scatter of measurements.

	LowHI	HighHI
Mean height of welding passes (mm)	3.2 (± 0.3)	3.5 (± 0.4)
Estimated temperature corresponding to the columnar/equiaxed transition for austenite grains in the region affected by the last pass - Rosenthal model (°C)	970 (± 50)	965 (± 50)
Average distance between the top boundary of the white bands and the fusion line of its affecting pass (mm)	3.2 (± 0.3)	3.7 (± 0.3)
Estimated peak temperature corresponding to the top of the white bands according to the Rosenthal model (°C)	750 (± 30)	770 (± 30)

3.2 Microstructural development

3.2.1 Microstructure of as-received welds

3.2.1.1 LowHI weld

In the last pass, the final microstructure was martensitic (M) with some retained austenite (RA) between and inside martensite blocks, regardless of the solidification mode (columnar vs. equiaxed) (Figure 9(a)). In the zone reheated by the last pass, having experienced full austenitization as the last thermal cycle, the microstructure also remained martensitic regardless of the austenitic grain morphology (Figure 9(b) and (c)). The mean overall hardness of these regions was 408 HV_{0.3}.

In the white bands, the microstructure contained a higher fraction of retained austenite particles in comparison with the microstructure of the other regions (Figure 9(d)). The low thickness and curved shape of white bands did not allow quantification of retained austenite by e.g. X-ray diffraction in those regions, so that these trends mainly remained qualitative. Nevertheless, this observation is consistent with the partial austenitization heat cycle suggested by thermal analysis and with observations of macrographs (see previous section). These regions were associated with a lower hardness (362 HV_{0.3}).

The consequences of local chemical segregation were evidenced in all regions (Figure 9(e)), resulting in a locally finer microstructure, with more tightly aligned laths and more retained austenite. The spatial distribution of these particular microstructures was compared to the solidification structure of the same regions, as revealed with Béchet-Beaujard etching. As a result, these regions were identified as interdendritic regions during the weld solidification stage. Their characteristic microstructure could be related to higher contents in alloying elements such as Ni, Mn, Mo, Cr, and Si (as shown in Figure 7): in particular, Ni and Mn tend to increase the fraction of retained austenite [45] and promote lower temperature-transformation constituents.

3.2.1.2 HighHI weld

The microstructure of the HighHI weld was different from that of the LowHI weld, both in the last pass and in regions affected by the last pass. The microstructure was composed of high-temperature austenite decomposition products, such as granular bainite (GB) with islands of retained austenite (RA) and upper bainite (UB) (Figure 10(a)). Finer constituents such as martensite/lower bainite were also found (Figure 10(b)), probably due to local chemical segregation as already observed with the LowHI weld microstructure. The hardness of these two regions was 366 HV_{0.3}. The same microstructural constituents were found in the white bands, with a (qualitatively) higher fraction of retained austenite. The hardness of white bands was slightly lower (359 HV_{0.3}).

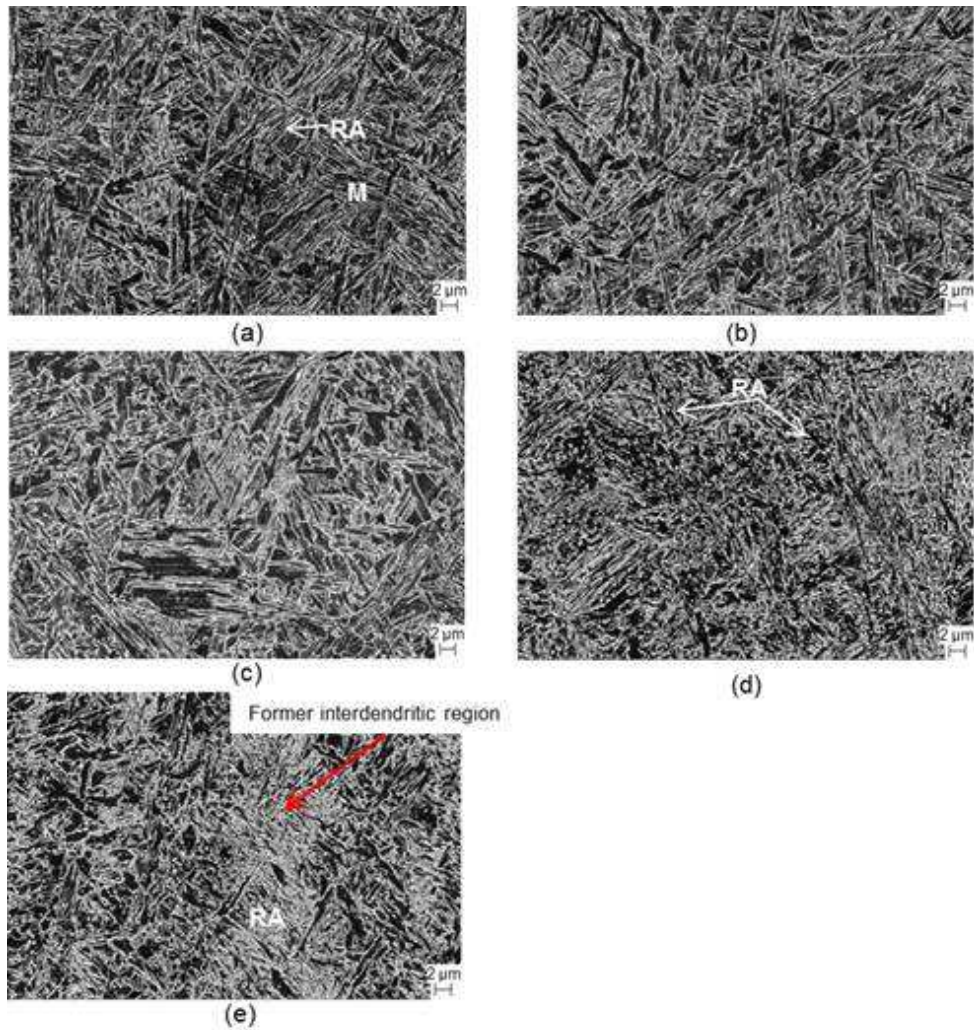


Fig. 9 – SEM micrographs of the LowHI weld after nital etching; (a) as-deposited columnar microstructure, (b) and (c) region affected by the last pass, respectively, in zones of equiaxed and columnar austenitic grains, (d) white band microstructure, (e) local microstructural heterogeneity inherited from microsegregations during solidification

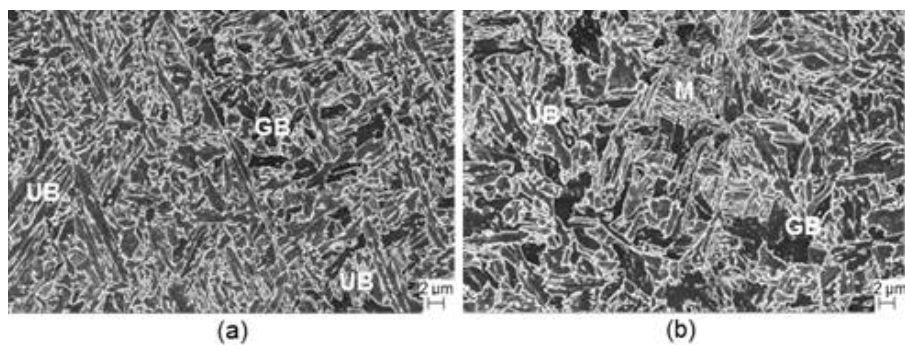


Fig. 10 – SEM micrographs of the HighHI weld after nital etching; (a) as-deposited microstructure, (b) equiaxed-austenite zone in the region affected by the last pass.

3.2.2 Investigation of microstructural development with laboratory heat cycles

The specimen geometry ensured the presence of both columnar and equiaxed zones in any section before the laboratory heat cycle (Figure 11(a)), so that they were searched for after the heat cycle as well. Figure 11(b) and (c) also show the microstructures obtained after two laboratory heat cycles up to T_{peak} above A_{c3} .

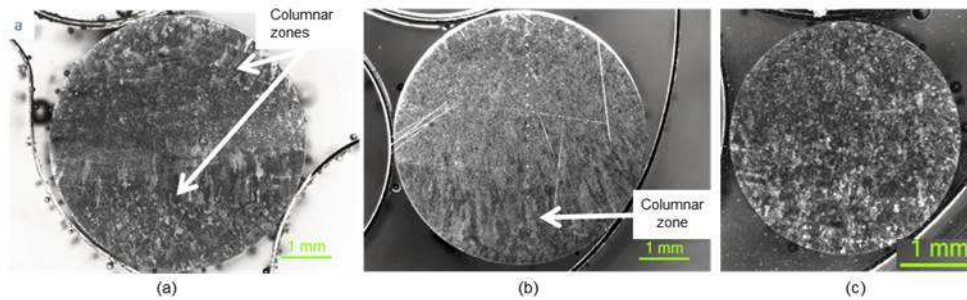


Fig. 11 – Laboratory specimen macrographs in cross-section, (a) in the as-welded state and (b, c) after heat cycles with $T_{\text{peak}} = 870^{\circ}\text{C} = A_{c3} + 30^{\circ}\text{C}$ (b) and $T_{\text{peak}} = 1050^{\circ}\text{C} = A_{c3} + 210^{\circ}\text{C}$ (c). Nital etching, the welding direction is perpendicular to the images.

After a cycle up to $T_{\text{peak}}=870^{\circ}\text{C}$ (Figure 11(b)), a columnar zone was still present; but after cycling up to $T_{\text{peak}}=1050^{\circ}\text{C}$ (Figure 11(c)), the columnar zones were replaced by equiaxed austenitic grains all over the section of the specimen. Therefore, with increasing T_{peak} above A_{c3} , there was a progressive disappearance of columnar zones after one heat cycle. This result confirms the hypothesis of a memory effect of initial austenite grains.

The presence of retained austenite, between the laths, in the weld microstructure seemed to physically allow this austenite memory phenomenon. To validate this hypothesis, two experimental cycles with partial austenitization were performed, namely, one at $T_{\text{peak}}=720^{\circ}\text{C}$ (close to A_{c1}) and another one at $T_{\text{peak}}=805^{\circ}\text{C}$ (close to A_{c3} but still in the intercritical range).

After cycling up to 720°C , the final microstructure was similar to the initial one and retained austenite had not evolved (Figure 12(a) and (d)). By increasing the peak temperature up to 805°C (closer to A_{c3}), the resulting microstructure (Figure 12(b), (e)) became closer to the one after a heat cycle up to 870°C (Figure 12(c) and (f)). In addition, the fraction of retained austenite particles with acicular shapes appeared qualitatively higher after a high temperature intercritical heat cycle (Figure 12(e)) than without significant austenitization (Figure 12(d)).

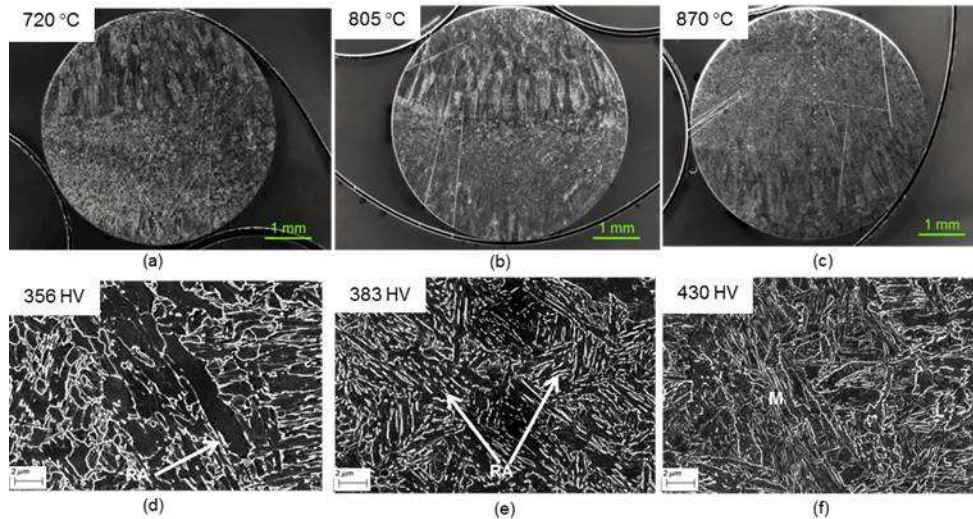


Fig. 12 – (a-c) Macrographs and (d-f) SEM micrographs after partial re-austenitization up to 720°C (a,c) and 805°C (b,d) and after full austenitization (c,f).

After full austenitization, the final microstructure strongly depended on the peak temperature. For lower values of T_{peak} (here, 870°C), the final microstructure was martensitic, with a low transformation start temperature (402 °C) and a high hardness (Figure 12(f)). The microstructure was the same, whatever being formed from the decomposition of columnar or of equiaxed austenitic grains (Figure 12(c)). By raising the peak temperature up to 1050 °C, the final microstructure became bainitic-martensitic with the presence of retained austenite (Figure 13). The hardness was lower (364 HV_{0.3}) and the start temperature of the austenite transformation on cooling, Ar_3 , was higher. These data are gathered in Table IV.

Table IV - Comparison between the laboratory heat cycles: resulting hardness, starting point of austenite decomposition and resulting fractions of bainite and martensite as determined from dilatometry.

T_{peak} (°C)	720 °C	805 °C	870 °C	1050 °C
Cooling scheme	12 °C/s + 5 °C/s	12 °C/s + 5 °C/s	12 °C/s + 5 °C/s	12 °C/s + 5 °C/s
Hardness (HV _{0.3})	356 (± 9)	383 (± 11)	430 (± 6)	364 (± 14)
Ar_3 (°C)	-	-	402	466
Bainite fraction	-	-	0	53
Martensite fraction	-	-	100	47

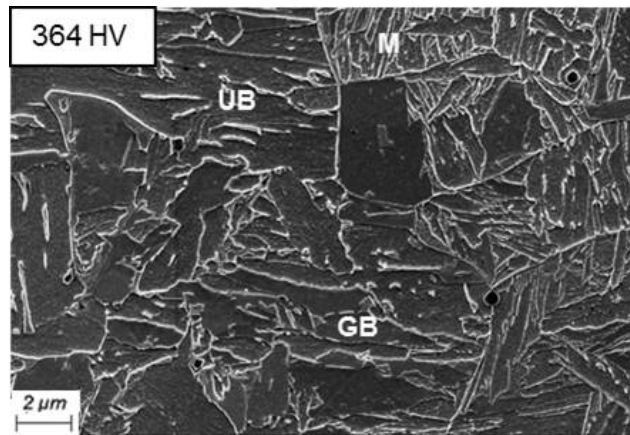


Fig. 13 – SEM micrograph after a laboratory heat cycle with $T_{\text{peak}} = 1050 \text{ }^{\circ}\text{C}$, nital etching.

4 Discussion

4.1 Origin and persistence of the austenite memory effect

Laboratory heat cycles up to different peak temperatures revealed the progressive disappearance of the columnar austenitic grains with increasing peak temperature in the fully austenitic domain. Thus, there was a memory of the shape of initial austenitic grains, which explains the presence of columnar zones (and thus, of grain morphology reminiscent of that resulting from metal deposition) and the presence of fine equiaxed zones in macrographs. This alternation between two types of austenite grain morphology was directly related to the different austenitization cycles caused by the subsequent passes.

Intercritical annealing cycles (Figure 12) showed the evolution of the microstructure during phase transformation, namely, growth of retained austenite between the laths for T_{peak} approaching A_{c3} . This tends to prove that during heating, the growth of austenite between martensitic or bainitic laths was the main reverse transformation mechanism.

Regarding reverse transformation of martensite or bainite into austenite, no information was available from open literature concerning weld metals. Out of welds, several authors reported the presence of two different families of retained austenite particles: globular ones and acicular ones [35-39,42,48]. Globular austenite particles were mostly located at initial austenite grain boundaries whereas acicular particles simply grew at martensite or bainite lath boundaries. Even after further growth, acicular (reverted) austenite particles still possessed the crystal orientation of the initial austenite grain. Thus, reconstitution of initial austenite grains during reheating was attributed to the growth and impingement of acicular austenite particles.

In the present microstructures, retained austenite was localized between the laths and possessed an elongated (acicular) shape. Therefore, the presence of elongated retained austenite after an intercritical annealing seemed to provide austenite memory, as reported in literature for non-welded metals (see above). On the other hand, austenite memory from diffusional growth of retained austenite was only reported so far with low heating rates, namely, between 10 and 1000 $^{\circ}\text{C}/\text{min}$ (i.e., between 0.167 and 16.7 $^{\circ}\text{C}/\text{s}$) [33,42,49]. In the present study, austenite memory came together with higher

heating rates (more than 50°C/s); such circumstances are often associated with diffusionless shear mechanism. [39,50,51]

After a high- T_{peak} thermal cycle, the columnar austenitic morphology was replaced by an equiaxed morphology with a finer austenite grain size. Several authors reported about austenite grain refinement occurring upon further heating, *after* completion of the austenite memory phenomenon [30,31,48,50]. This involved nucleation of *new* austenite grains that differ from initial austenite grains. Globular austenite particles were reported to mostly nucleate at PAGBs, simultaneously with the growth of elongated particles [35-39,42,48]. Elongated austenite particles possessed the initial austenite grain orientation, whereas the crystal orientation of globular austenite differed from those of neighboring initial austenite grains [38,47]. Upon heating, austenite memory relied on preferential growth and merging of elongated austenite particles into initial austenite grains, even if in competition with globular ones, up to full austenitization. At higher temperatures, globular grains might start to significantly grow and to progressively replace coarse initial austenite grains by a fine, equiaxed austenite grain structure. This grain refinement phenomenon is somewhat similar to recrystallization. The physical phenomenon leading to the growth of finer, newly nucleated austenite grains could be linked to a diffusionless austenite reversion mechanism from acicular particles [31,50,51]. During their growth into bainite or martensite, especially at high heating rates, elongated austenite particles could have inherited from defects (here, dislocations) from the neighboring laths. On the other hand, globular austenite grains, having no orientation relationship with the neighboring crystals [38,48], probably grew by a purely diffusional mechanism, without inheritance of such defects. They might have started to grow more slowly than elongated austenite particles, but with a lower density of internal defects. On the other hand, they might possess a higher (incoherent) grain boundary mobility at higher temperatures than austenite particles growing between the laths. These differences between austenite grains originated from globular and elongated particles, respectively, might provide a sufficiently high driving force for subsequent growth of (finer) globular austenite grains at the expense of (coarser) initial ones, *after full reversion into austenite*. Even under lower heating rates, Shinozaki et al. [48] proposed such a mechanism to explain the growth of globular grains. Thus, in the present case, rapid heating rates could promote a sufficient density of dislocations to trigger grain refinement when the peak temperature is higher than 970°C.

This so-called “austenite grain refinement” scenario was confirmed by the austenitic grain morphology of laboratory specimens heated up to 805 °C and 870 °C. In Figure 14, the differences in austenite grain morphology after $T_{\text{peak}}=870$ °C, between an initial equiaxed zone and an initial columnar zone, appeared as follows:

- In equiaxed zones, only equiaxed grains with a smaller size than the initial ones were found (Figure 14(a)). This was confirmed by EBSD maps (Figure 14(c)) showing randomly oriented crystals suggesting small randomly-oriented austenitic grains (5-10 μm), as those found in the optical micrographs (Figure 14(a));
- In columnar zones, small equiaxed grains were found at boundaries of the columnar austenite grains still present after austenitization (Figure 14(b)). In EBSD maps, regions with the same equiaxed microstructure as above were found at boundaries of columnar austenitic grains in the former columnar zone (Figure 14(d)).

From these observations, after full austenitization up to $A_{c3}+30^\circ\text{C}$, austenite memory was still present in macrographs; yet, the competition between growth and merging of retained austenite into initial grains, and growth of equiaxed grains from initial PAGBs was demonstrated. The latter phenomenon

tended to replace initial columnar grains upon further increase in T_{peak} . These observations are thus in agreement with literature findings on non-welded materials and strongly support this scenario in the investigated welds. To evaluate this competition even before full austenitization, the microstructure of the specimen heated up to $T_{\text{peak}}=805^{\circ}\text{C}$ was further characterized (Figure 15). Figure 15(c) and (d) provide the same conclusion as with the 870°C specimen, showing that even when the specimen temperature was still in the intercritical range, competitive growth of elongated retained austenite particles (leading to columnar austenite grains) and of newly nucleated globular austenite (leading to smaller, equiaxed austenite grains) was already active.

The proposed interpretation of the mechanism of austenite memory from retained austenite is summarized in Figure 16. The differences between equiaxed and columnar regions based on the experimental observations are presented.

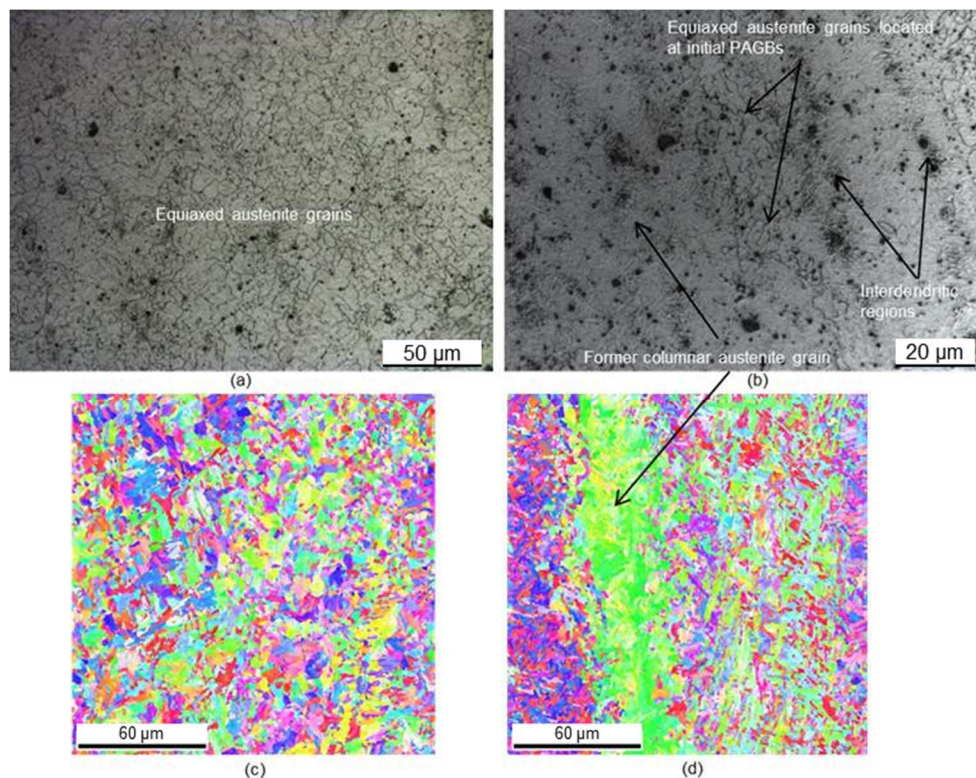


Fig. 14 – Optical micrographs after a Béchet-Beaujard etching and EBSD maps of a laboratory specimen after a heat cycle up to 870°C . (a) Presence of small austenite grains in an initial equiaxed zone. (b) Presence of initial columnar austenite grains together with small equiaxed ones at initial PAGBs. Austenite grain boundaries are delineated by thin lines. Darker regions are linked to interdendritic segregations. (c) and (d) EBSD inverse pole figure maps (sample normal= welding direction) in a equiaxed zone (c) and in a columnar zone (d).

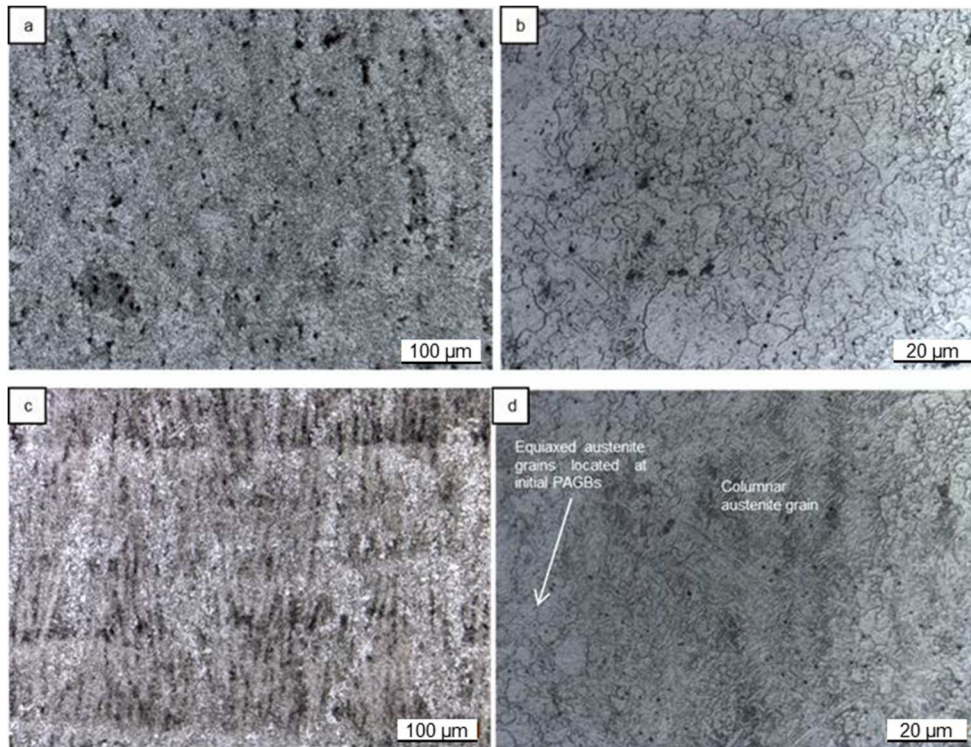


Fig. 15 – Optical micrographs after a laboratory heat cycle up to 805°C. (a) and (b) Initial equiaxed zone where only small equiaxed austenite grains were formed. (c) and (d) Initial columnar zone with columnar austenite grains, together with smaller equiaxed austenite grains located at initial PAGBs. (a, c) Béchet-Beaujard etching showing the solidification structure and (b, d) showing the austenite grain morphology.

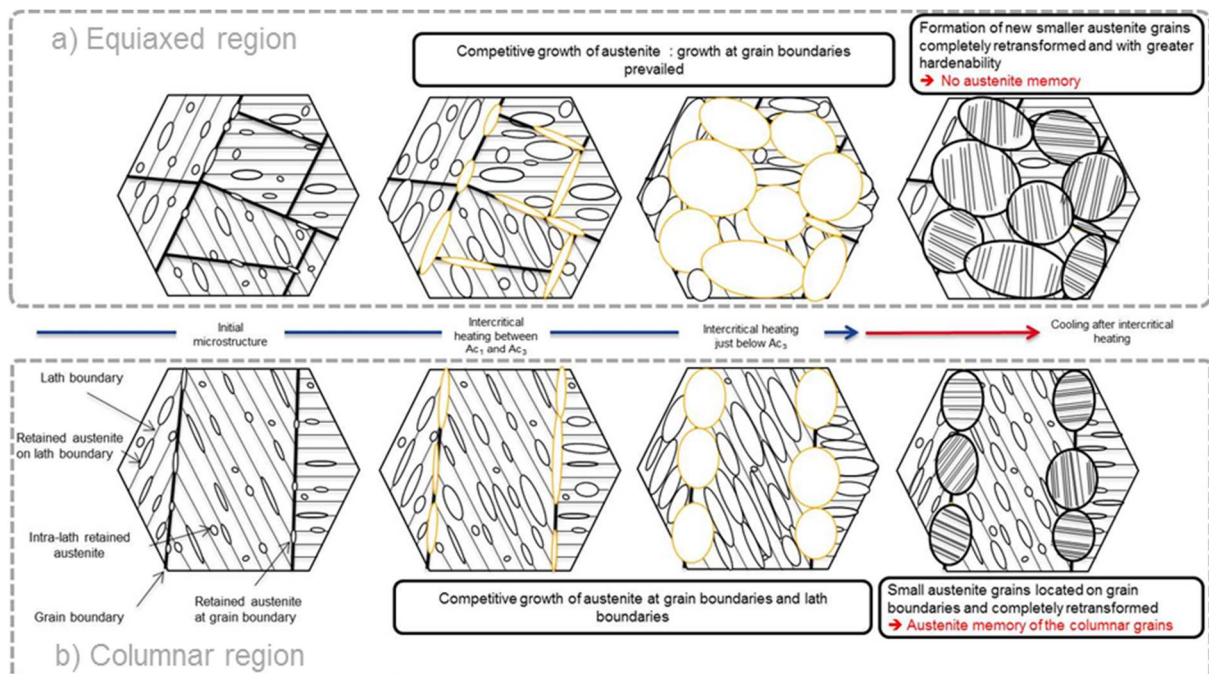


Fig. 16 - Schematic representation of the austenite memory mechanism in the investigated low alloy steel welds. Thin lines delineate lath boundaries. Thick black lines delineate the boundary of former and newly grown austenite grains that further decomposed into a lath-like microstructure during cooling. For clarity, austenite grains formed from the nucleation and growth of globular particles are represented in orange. The competitive growth of austenite grains formed from acicular and globular austenite particles differs in (a) equiaxed and (b) columnar initial austenite regions.

4.2 Origin and properties of white bands

The study of the white bands was based on the laboratory intercritical heat cycles. In the weld, the microstructure in the white bands contained a large proportion of retained austenite (Figure 4(d)); it was often associated with a lower hardness. Comparison of as-welded white bands with laboratory-treated microstructures (Figure 12(e)) revealed great similarities. In agreement with assumptions suggested by thermal modeling, white bands observed in macrographs were assimilated to regions where final austenitization was significant, but only partial. The lower boundary of the white bands was blurred because the enrichment in retained austenite progressively appeared with increasing T_{peak} . Consequently, the iso- $T_{\text{peak}}=Ac_1$ line could not be accurately compared to the lower boundary of white bands, whereas the upper boundary of white bands well matched the iso- $T_{\text{peak}}=Ac_3$ line.

White bands have also been investigated in a HSLA-100 weldment [52]; they were curved and associated with the so-called HAZ of the corresponding affecting pass. They possessed lower hardness than the martensitic microstructure of the remaining weld metal, and a lath ferrite microstructure with some retained austenite. The predominance of lath ferrite instead of martensite, and of a small amount of retained austenite in these white bands was attributed to a low- T_{peak} reheating cycle, within or directly above the intercritical range, and to a relatively slow cooling rate. The present findings are in agreement with these results, at least, for the peak temperature range.

The lower hardness of white bands (- 46 HV_{0.3} in LowHI and - 7 HV_{0.3} in HighHI), compared to the material next to them, could possibly be attributed to (a) extensive recovery of untransformed martensite (or bainite) during the intercritical heat cycle and (b) to the presence of retained austenite that could induce some transformation-induced plasticity effects during the hardness testing. Further work is required to elucidate these contributions in more detail.

4.3 Influence of the peak temperature on the final microstructure in the case of full austenitization

In both the laboratory heat treated specimens and the investigated as-welded materials, the peak temperature had a strong influence on the final microstructure. For lower peak temperatures ($>Ac_3$), the final microstructure was harder (430 HV_{0.3}) and fully martensitic. For higher peak temperatures ($>>Ac_3$), the microstructure was bainitic-martensitic with a lower hardness (364 HV_{0.3}). The influence of this parameter on the final microstructure has been extensively reported in literature, yet, mostly in the HAZ. Simulated heat cycles were applied to obtain different microstructures with different prior austenite grain sizes [21,22,55,56]. No clear relationship was established between the prior austenite grain size and the final microstructure. In fact, some studies revealed that in coarse grained regions, the microstructure was harder, coming along with the formation of lower transformation temperature constituents [21,22,53] but the opposite effect was also reported [54-56]. Similar discrepancies were reported regarding the dependence of M_s (martensite start temperature) and B_s (bainite start temperature) temperatures upon the parent austenite grain size [53-56].

In the present case, the harder microstructure after low- T_{peak} heat cycles could be related to the appearance of those small austenite grains appeared at initial PAGBs (Figure 14 and Figure 15). By looking more closely at columnar regions, these small austenitic grains appeared brighter in optical micrographs (Figure 15(a)) than the columnar grains themselves. This suggests a lower fraction of retained austenite in those grains. The microstructure after the 805 °C heat cycle (Figure 17) confirmed a strong inheritance from the duplex austenitic grain morphology. In columnar (initial)

austenite grains, a significant fraction of elongated retained austenite was found after cooling, indicating an incomplete decomposition of austenite upon final cooling. Conversely, small equiaxed austenite grains completely transformed into martensite, without visible retained austenite, upon cooling. These small austenite grains possessed higher hardenability than columnar grains. To confirm the contribution of the prior austenite grain size on the final decomposition of austenite, two microstructures obtained after identical cooling conditions were compared, namely, laboratory specimens respectively heat-treated up to 870 °C and 1050 °C. The great majority of the 870 °C specimen transformed into small equiaxed austenite grains (5-10 μm) during heating. Its final microstructure was harder (430 HV_{0,3}) in comparison to the 1050 °C specimen (364 HV_{0,3}), where equiaxed austenitic grains became larger (18 μm), with lower hardenability.

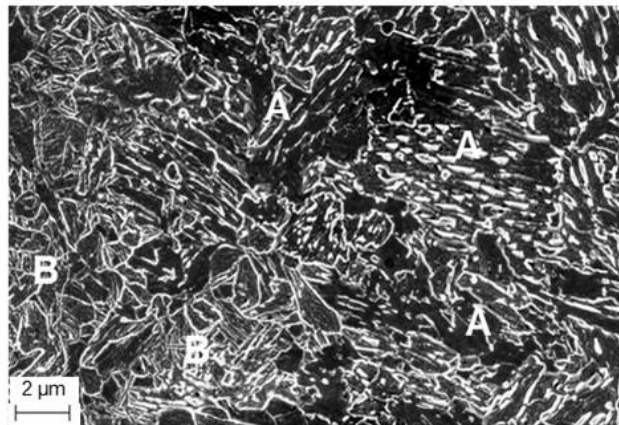


Fig. 17 – SEM micrograph illustrating the duplex microstructure after a partial austenitization up to 805°C. Incomplete decomposition of columnar, coarse-grained austenite (A) and complete martensitic transformation of smaller, equiaxed austenite grains (B).

5 Conclusions

For the first time, a methodology combining a simplified thermal model and a dedicated experimental campaign was adopted to elucidate the influence of local thermal cycles on the macrostructure and microstructure of the weld metal of multipass welded joints. This methodology could readily be extended to non-welded materials. In the investigated welds, the following results were obtained:

- The alternation of columnar and equiaxed austenitic regions all over the multipass weld could be explained by the effect of the local peak temperature on the austenite memory phenomenon. This memory effect disappeared at peak temperatures higher than $A_{c3} + 130^{\circ}\text{C}$.
- In the case of full austenitization, the lower the peak temperature, the higher the hardness of the final microstructure, regardless of the occurrence of austenite memory.
- The austenite memory phenomenon was linked to the growth, then the merging of elongated retained austenite particles located between the laths. These particles kept the crystal orientation of initial austenite grains. The austenite memory effect tended to disappear with the increase in peak temperature, due to replacement of these austenite grains by those grown from globular, incoherent grains located at initial PAGBs.
- White bands revealed in Béchet-Beaujard macrographs contained a higher fraction of retained

austenite and possessed lower hardness, possibly due to extensive matrix recovery and to the presence of retained austenite. All of them experienced intercritical annealing as the last thermal cycle involving austenitization.

Acknowledgements

The authors greatly acknowledge the French National Association for Research and Technology (ANRT) for financial support under CIFRE Grant no. 2018/1249. The authors warmly thank Gérard Brabant (Centre des Matériaux) for his kind help and assistance with dilatometric tests.

Conflict of Interest

The authors declare that they have no conflict of interest.

References

1. R. E., Dolby: *Eng. Appl. Fract. Anal.*, 1980, pp. 117-34. <https://doi.org/10.1016/B978-0-08-025437-1.50017-6>
2. D. J. Abson and R. J. Pargeter: *Int. Met. Rev.*, 1986, vol. 31 (1), pp. 141-96. <https://doi.org/10.1179/imtr.1986.31.1.141>
3. E. Keehan, L. Karlsson, H. O. Andrén and L. E. Svensson: *Weld. J.*, 2006, vol. 85 (10), pp. 218-24.
4. E. S. Surian, N. M. Rissone, H. G. Svoboda and L. A. Vedia: *Weld. J.*, 2010, vol. 89 (3), pp. 54-64.
5. L. Lan, C. Qiu, D. Zhao, X. Gao and L. Du: *Mater. Sci. Eng., A*, 2011, vol. 529, pp. 192-200. <https://doi.org/10.1016/j.msea.2011.09.017>
6. B. C. Kim, S. Lee, N. J. Kim and D. Y. Lee: *Metall. Trans. A*, 1991, vol. 22 (1), pp. 139-49. <https://doi.org/10.1007/BF03350956>
7. S. Moeinifar, A. H. Kokabi and H. M. Hosseini: *Mater. Des.*, 2010, vol. 31 (6), pp. 2948-55. <https://doi.org/10.1016/j.matdes.2009.12.023>
8. D. Rosenthal: *Trans. ASME*, 1946, vol. 68, pp. 849-66.
9. N. N. Rykalin: *Calculation of heat processes in welding*, U.S.S.R, Moscow, 1960.
10. H. Arora, R. Singh and G. S. Brar: *Meas. Control*, 2019, vol. 52 (7-8), pp. 955-69. <https://doi.org/10.1177/0020294019857747>
11. M. J. Attarha and I. Sattari-Far: *J. Mater. Process. Technol.*, 2011, vol. 211 (4), pp. 688-94. <https://doi.org/10.1016/j.jmatprotec.2010.12.003>
12. E. Keehan, J. Zachrisson and L. Karlsson: *Sci. Technol. Weld. Joining*, 2010, vol. 15 (3), pp. 233-38. <https://doi.org/10.1179/136217110X12665048207692>
13. G. Mao, R. Cao, C. Cayron, X. Mao, R. Logé and J. Chen: *Mater. Sci. Eng. A*, 2019, vol. 744, pp. 671-81. <https://doi.org/10.1016/j.msea.2018.12.035>
14. R. W. Fonda and G. Spanos: *Metall. Mater. Trans. A*, 2000, vol. 31 (9), pp. 2145-53. <https://doi.org/10.1007/s11661-000-0132-0>
15. M. Lord and G. Jennings: *Svetsaren* (Swed. Ed.), 1999, vol. 54 (1-2), pp. 53-58.

16. M. Q. Johnson, G. M. Evans and G. R. Edwards: *Metals*, 1995, vol. 35 (10), pp. 1222-31. <https://doi.org/10.2355/isijinternational.35.1222>
17. B. Dixon and K. Hakansson: *Weld. J.*, 1995, vol. 74 (4), pp. 122-32.
18. X. F. Zhang, P. Han, H. Terasaki, M. Sato and Y. Komizo: *J. Mater. Sci. Technol.*, 2012, vol. 28 (3), pp. 241-48. [https://doi.org/10.1016/S1005-0302\(12\)60048-6](https://doi.org/10.1016/S1005-0302(12)60048-6)
19. Y. Kang, G. Park, S. Jeong and C. Lee: *Metall. Mater. Trans. A*, 2018, vol. 49 (1), pp. 177-86. <https://doi.org/10.1007/s11661-017-4384-3>
20. R. Mythili, V. T. Paul, S. Saroja, M. Vijayalakshmi and V. S. Raghunathan: *J. Nucl. Mater.*, 2003, vol. 312 (2-3), pp. 199-206. [https://doi.org/10.1016/S0022-3115\(02\)01680-X](https://doi.org/10.1016/S0022-3115(02)01680-X)
21. M. Shome, O. P. Gupta and O. N. Mohanty: *Metall. Mater. Trans. A*, 2004, vol. 34 (13), pp. 985-96. <https://doi.org/10.1007/s11661-004-1002-y>
22. G. Spanos, R. W. Fonda, R. A. Vandermeer and A. Matuszeski: *Metall. Mater. Trans. A*, 1995, vol. 26 (12), pp. 3277-93. <https://doi.org/10.1007/BF02669455>
23. E. S. Surian and L. A. De Vedia: *Weld. J.*, 1999, vol. 78, pp. 217-28.
24. M. M. Amrei, H. Monajati, D. Thibault, Y. Verreman, L. Germain and P. Bocher: *Mater. Charact.*, 2016, vol. 111, pp. 128-36. <https://doi.org/10.1016/j.matchar.2015.11.022>
25. W. Liu, F. Lu, Y. Wei, Y. Ding, P. Wang and X. Tang: *Mater. Des.*, 2016, vol. 108, pp. 195-206. <https://doi.org/10.1016/j.matdes.2016.06.102>
26. A. J. M. Gomes, J. C. F. Jorge, L. F. G. de Souza and I. D. S. Bott: *Mater. Sci. Forum*, 2013, vol. 758, pp. 21-32. <https://doi.org/10.4028/www.scientific.net/MSF.758.21>
27. A. P. Gerlich, H. Izadi, J. Bundy and P. F. Mendez: *Weld. J.*, 2014, vol. 93 (1), pp. 15-22.
28. C. F. Jorge, J. L. D. Monteiro and A. J. Gomes: *J. Mater. Res. Technol.*, 2018, vol. 8 (1), pp. 561-71. <https://doi.org/10.1016/j.jmrt.2018.05.007>
29. Z. Zhang and R. A. Farrar: *Weld. J.*, 1997, vol. 76 (5), pp. 183-96.
30. G. Krauss JR: *Acta Metall.*, 1963, vol. 11 (6), pp. 499-509. [https://doi.org/10.1016/0001-6160\(63\)90085-3](https://doi.org/10.1016/0001-6160(63)90085-3)
31. H. Shirazi, G. Miyamoto, S. H. Nedjad, T. Chiba and M. N. Ahmadabadi: *Acta Mater.*, 2018, vol. 144, pp. 269-80. <https://doi.org/10.1016/j.actamat.2017.10.068>
32. N. Nakada, T. Tsuchiyam, S. Takaki, S. Hashizume: *ISIJ Int.*, 2007, vol. 47 (10), pp. 1527-32. <https://doi.org/10.2355/isijinternational.47.1527>
33. L. Liu, Z. G. Yang, C. Zhang and W. B. Liu: *Mater. Sci. Eng. A*, 2010, vol. 527 (27-28), pp. 7204-09. <https://doi.org/10.1016/j.msea.2010.07.083>
34. D. Brandl, M. Lukas, M. Stockinger, S. Ploberger and G. Ressel: *Mater. Des.*, 2019, vol. 176, 107841. <https://doi.org/10.1016/j.matdes.2019.107841>
35. T. Hara, N. Maruyama, Y. Shinohara, H. Asahi, G. Shigesato, M. Sugiyama and T. Koseki: *ISIJ Int.*, 2009, vol. 49 (11), pp. 1792-1800. <https://doi.org/10.2355/isijinternational.49.1792>
36. A. E. Nehrenberg: *J. Met.*, 1950, vol. 2 (1), pp. 162-74. <https://doi.org/10.1007/BF03398992>

37. S. Matsuda and Y. Okamura: *Trans. Iron Steel Inst. Jpn.*, 1974, vol. 14 (5), pp. 363-68.
<https://doi.org/10.2355/isijinternational1966.14.363>
38. X. Zhang, G. Miyamoto, T. Kaneshita, Y. Yoshida, Y. Toji and T. Furuhashi: *Acta Mater.*, 2018, vol. 154, pp. 1-13. <https://doi.org/10.1016/j.actamat.2018.05.035>
39. J. Han and Y. K. Lee: *Acta Mater.*, 2014, vol. 67, pp. 354-61.
<https://doi.org/10.1016/j.actamat.2013.12.038>
40. S. Watanabe and T. Kunitake: *Trans. Iron Steel Inst. Jpn.*, 1976, vol. 16 (1), pp. 28-35.
<https://doi.org/10.2355/isijinternational1966.16.28>
41. X. Zhang, G. Miyamoto, Y. Toji and T. Furuhashi: *Metals*, 2019, vol. 9 (2), pp. 266-74.
<https://doi.org/10.3390/met9020266>
42. S. T. Kimmins and D. J. Gooch: *Met. Sci.*, 1983, vol. 17 (11), pp. 519-32.
<https://doi.org/10.1179/030634583790420484>
43. P. Promopattum, S. C. Yao, P. C. Pistorius and A. D. Rollett: *Engineering*, 2017, vol. 3 (5), pp. 685-94. <https://doi.org/10.1016/J.ENG.2017.05.023>
44. L. M. Dong, X. B. Qiu, T. Y. Liu, Z. Y. Lu, F. Fang and X. J. Hu: *J. Mater. Sci. Eng. B*, 2017, vol. 7 (11-12), pp. 258-67. <https://doi.org/10.17265/2161-6221/2017.11-12.003>
45. E. Keehan, L. Karlsson, H. O. Andrén and H. K. D. H. Bhadeshia: *Sci. Technol. Weld. Joining*, 2006, vol. 11 (1), pp. 9-18. <https://doi.org/10.1179/174329306X77849>
46. N. Jousset, PhD Thesis, Université PSL, Paris, France, 2022.
47. S. Zajac, V. Schwinn, K. H. Tacke: *Mater. Sci. Forum*, 2005, vol. 500-501, pp. 387-94.
<https://doi.org/10.4028/www.scientific.net/MSF.500-501.387>
48. T. Shinozaki, Y. Tomota, T. Fukino and T. Suzuki: *ISIJ Int.*, 2017, vol. 57, pp. 533-39.
<https://doi.org/10.2355/isijinternational.ISIJINT-2016-557>
49. L. Liu, Z. G. Yang, C. Zhang and W. B. Liu: *Mater. Sci. Eng. A*, 2010, vol. 527 (27-28), pp. 7204-09. <https://doi.org/10.1016/j.msea.2010.07.083>
50. N. Nakada, R. Fukagawa, T. Tsuchiyama, S. Takaki, D. Ponge and D. Raabe: *ISIJ Int.*, 2013, vol. 53 (7), pp. 1286-88. <https://doi.org/10.2355/isijinternational.53.1286>
51. P. Song, W. Liu, C. Zhang, L. Liu and Z. Yang: *ISIJ Int.*, 2016, vol. 56 (1), pp. 148-53.
<https://doi.org/10.2355/isijinternational.ISIJINT-2015-280>
52. D. W. Moon, R. W. Fonda and G. Spanos: *Weld. J.*, 2000, vol. 79 (10), pp. 278-85.
53. S. Yamamoto, H. Yokoyama, K. Yamada and M. Niikura: *ISIJ Int.*, 1995, vol. 35 (8), pp. 1020-26.
<https://doi.org/10.2355/isijinternational.35.1020>
54. L. Lan, Z. Chang and P. Fan: *Metals*, 2018, vol. 8 (12), pp. 988-100.
<https://doi.org/10.3390/met8120988>
55. S. J. Lee, J. S. Park and Y. K. Lee: *Scr. Mater.*, 2008, vol. 59 (1), pp. 87-90.
<https://doi.org/10.1016/j.scriptamat.2008.02.036>
56. S. J. Lee and Y. K. Lee: *Mater. Sci. Forum*, 2005, vol. 475, pp. 3169-72.
<https://doi.org/10.4028/www.scientific.net/MSF.475-479.3169>